Effect of Y-additions on the oxidation behavior of novel refractory high-entropy alloy NbMoCrTiAl at 1000°C in air

Authors

Franz Müller[a], Bronislava Gorr[a], Hans-Jürgen Christ[a], Hans Chen[b], Alexander Kauffmann[b] and Martin Heilmaier[b]

Affiliation

[a]Institut für Werkstofftechnik, Universität Siegen, Siegen, Germany; [b]Institut für Angewandte Materialien, Karlsruher Institut für Technologie (KIT), Karlsruhe, Germany

Abstract

In this work, the influence of 0.5 at.% and 1 at.% Y additions on the high temperature oxidation resistance of the equiatomic alloy NbMoCrTiAl at 1000°C in air was investigated. Continuous isothermal and cyclic thermogravimetric experiments (TGA) were conducted to characterize the oxidation kinetics of the alloys. Various analytical methods such as X-ray diffraction (XRD) and electron microscopy (SEM) with energy-dispersive X-ray spectroscopy (EDX) were used to study the growth, morphology and composition of the oxide scales. It was found that the Y-additions led to the formation of Al_2Y phase along grain boundaries. The isothermal oxidation experiments of both Y-containing alloys showed lower oxidation rates after a short period of transient oxidation probably due to a reduction of fast growing and voluminous Nb_2O_5 oxides within the oxide layer. During the steady-state period, however, oxidation of Al_2Y caused local stresses resulting in crack formation and subsequent breakaway oxidation, i.e. pronounce increase of the oxidation rates. The cyclic oxidation experiments revealed lower oxidation rates and thinner, more adherent oxide scales formed on the alloy NbMoCrTiAl1Y compared to NbMoCrTiAl. The increased scale adherence was attributed to the formation of pegs due to the oxidation of Al_2Y phase at the oxide/metal interface.

Keywords: High-Entropy Alloys, Refractory metals, Y-Effect, Reactive element effect, Pegs

Introduction

Following the most innovative concepts in material science in the last decades, i.e. High Entropy Alloys (HEAs) [1], a huge number of new alloys have been manufactured and some have shown exceptional or unexpected properties [2–4]. On the basis of the HEA concept, refractory high entropy alloys (RHEAs) with promising mechanical properties for high temperature applications have been designed [5–9]. Most of the RHEAs, however, possess poor oxidation resistance because of the high amount of refractory metals [4, 5, 10, 11]. The classic approach to improve the oxidation behavior of high temperature materials is with the addition of Cr, Al or Si, i.e. that allow the formation of potentially protective scales Cr_2O_3, Al_2O_3 and SiO_2 [12–14]. The identification of proper concentrations of Cr, Al or Si is usually a challenging task, since high concentrations of these elements ensure the formation of protective oxide scales on the one hand. On the other hand, they typically lead to formation of undesired intermetallic phases such as Laves, sigma as well as aluminides and silicides.

Rare-earth element additions of Y, Ce, La etc. may potentially increase the high-temperature oxidation resistance of alloys and allow to keep the concentrations of Cr, Al or Si on a moderate level. Small additions of Y, for example, were reported to increase oxidation resistance of various alloys by: (i) reduction in the scale growth rate, (ii) change in the scale growth mechanism, (iii) decreasing oxide scale spallation and (iv) increasing the plasticity of the oxide scale through grain refinement [15–17]. In particular, the beneficial effect of Y on the oxidation resistance of Ti-Al and Nb-Ti-Al alloys was demonstrated. It was shown that with increasing Nb content higher concentrations of Y are required, though Y concentrations above 0.3 at.% should be avoided due to the excessive formation of intermetallic compounds like Al_2Y that lead to embrittlement [18–21]. Al_2Y with C15-type crystal structure, however, also has a positive impact by increasing the oxide scale adherence through the formation of pegs [18–21]. Although the effect of rare-earth elements has been extensively investigated in common high-temperature materials, no studies have been reported out for RHEAs to the best of the authors' knowledge.

Our previous research on microstructure and high temperature corrosion behavior of the equiatomic RHEA NbMoCrTiAl revealed a multi-component microstructure containing a B2 ordered matrix phase with small volume fractions (<0.5 vol.%) of Cr_2Nb Laves phase (C14 type) and $Al(Mo,Nb)_3$ phase (A15 type) located predominately at grain boundaries [22–24]. A moderate oxidation resistance of this alloy was observed in the temperature range from 900 to 1100°C [22, 25]. No continuous, protective scales form on the metallic surface. Instead, rather thick and porous layers consisting of mixed rutile- and corundum-type oxides were observed [22, 25]. It is clear that the intrinsic oxidation resistance of this alloy should be improved by modification of its chemical composition, e.g. by Y additions. In this contribution, new selected results on the equiatomic RHEA NbMoCrTiAl are presented. The focus of this study is to explore the effect of 0.5 and 1 at.% Y additions to the equiatomic alloy on the isothermal and cyclic oxidation behavior and to identify the associated oxidation mechanism.

Experimental Procedures

The present study deals with the equimolar reference alloy NbMoCrTiAl and two additional alloys which were modified by 0.5 at.% or 1 at.% Y-additions and which are designated as NbMoCrTiAl0.5Y and NbMoCrTiAl1Y. All alloys were cast from elemental bulk materials by arc-melting (arc-melter AM 0.5 by Edmund Bühler GmbH) in ~0.6 atm. Ar. Before melting the elements the residual oxygen within the processing chamber was gettered by liquefying a Zr globule. The purities of the bulk materials Nb, Mo and Al were 99.9%, while Cr, Ti and Y had purities of 99.9 %, 99.8% and 99.9, respectively. The prepared buttons were flipped and remelted for at least five times in a water-chilled copper mold to facilitate alloy homogenization. All alloys were subsequently heat-treated at 1300 °C for 20 h in an Ar atmosphere (see Table 1) to remove the dendritic microstructure. The ingots were cut by electrical discharge machining (EDM) to dimensions of approximately 5 mm x 5 mm x 2 mm. The EDM surfaces polished up to grit 1200 and ultrasonically cleaned in ethanol directly before high temperature exposure to air.

Oxidation tests were carried out in a Rubotherm thermogravimetric system under isothermal and cyclic conditions at 1000°C in laboratory air. For the cyclic oxidation experiments, 20 cycles consisting of 1 h each at 1000°C in the furnace followed by rapid cooling at room temperature for 15 min in air were conducted.

To analyse the oxide morphology, a Focused Ion Beam - Scanning Electron Microscope (FIB-SEM) DualBeam system of type FEI Helios Nanolab 600 equipped with a backscatter electron (BSE) imaging detector as well as an energy-dispersive X-ray spectroscopy (EDX) were used. The crystal

structures of the samples and products within the thermally-grown scales were analysed by X-ray diffraction (XRD). For this, the samples were crushed to powders with particle sizes below 40 µm whereas the oxidized samples were measured as a bulk specimen without any additional preparation directly after exposure. The XRD measurements were conducted using an X'Pert Pro MPD diffractometer operating in Bragg-Brentano geometry with Cu-Kα radiation. A Ni-filter to decrease the beta radiation and divergence slits of 1 and 0.5° to achieve high intensities and resolutions was used. In addition, the step size was set to 0.01°/sec with an acquisition time of 45 s per step. The substrates and the oxide phases were identified by using the Inorganic Crystal Structure Database (ICSD) in the HighScore Software (Malvern Pananalytical).

Results

Microstructures

The microstructures of NbMoCrTiAl without and with additions of 0.5 at.% or 1 at.% Y after homogenization are shown in Fig. 1. As already presented in our previous studies [22, 23, 26], the microstructure of the alloy NbMoCrTiAl shows a B2-ordered matrix with two intermetallic phases of Cr_2Nb Laves and $Al(Mo, Nb)_3$ A15, which were identified to form predominately at the grain boundaries. XRD investigations of the Y-free and Y-containing alloys, which are displayed in Fig.2, clearly indicate the occurrence of a B2 super lattice peak for all alloys. In the Y-containing alloys, another Laves phase of C15-type was identified by means of XRD (Fig. 2). EDX analysis revealed a stoichiometry similar to Al_2Y (not shown here). As indicated in Fig. 1, the Al_2Y is predominantly formed at grain boundaries. In addition, minor amounts of C14-type Laves phase were observed predominantly at the grain-boundaries; the formation of the A15 phase, however, was not identified in both Y-added alloys. The volume fractions of the various phases were determined by areal analysis of BSE contrast images with ImageJ and are listed in Table 1. Obviously, the volume fraction of Al_2Y phase, was found to be higher in the alloy with 1 at. % Y than in the alloy containing 0.5 at.% Y (see Table 1).

Table 1: Designation of the investigated alloys, homogenization conditions, observed phases and their volume fraction determined.

alloy	**annealing conditions**	**identified phases**	**volume fractions**
NbMoCrTiAl	1300 °C, 20 h	Matrix (B2) $Al(Mo,Nb)_3$ (A15) Cr_2Nb (C14)	99% 0.5% 0.5%
NbMoCrTiAl0.5Y	1300 °C, 20 h	Matrix(B2) Cr_2Nb (C14) Al_2Y (C15)	97.25% <0.5% 2.25%
NbMoCrTiAl1Y	1300 °C, 20 h	Matrix (B2) Cr_2Nb (C14) Al_2Y (C15)	94.25% <0.5% 5.25%

Oxidation kinetics

In Fig. 3, the mass change curves of NbMoCrTiAl, NbMoCrTiAl0.5Y and NbMoCrTiAl1Y in (a) linear and (b) double-logarithmic plot during isothermal exposure to air at 1000°C are shown. Qualitatively, three distinctive stages can be recognized in each oxidation curve: (stage I) transient oxidation up to approximately 2 h with a strong increasing mass gain, (stage II) slow oxidation kinetics and (stage III) a strong increase of the oxidation rates. The mass change per unit area *(ΔW/A)* during isothermal oxidation over time can be explained as in equation (1) where n means the oxidation rate exponent, t time and k_n the oxidation constant. Using the double logarithmic plot of mass change versus time, the kinetic parameters, i.e., oxidation rate exponent n and oxidation constant k_n can be evaluated according to equation (2). The n and k_n values for the corresponding stages II and III of the oxidation curves shown in Fig. 3 are listed in Table 2.

$$(\Delta W/A)^n = k \cdot t \qquad (1)$$

$$\ln \Delta W/A = \frac{1}{n} \ln k_n + \frac{1}{n} \ln t \qquad (2)$$

During the transient oxidation (stage I), the mass gains of both Y-containing alloys are higher compared to that of the Y-free alloy. Stage II yields, on the contrary, lower oxidation rate exponents and longer durations for both alloys NbMoCrTiAl0.5Y and NbMoCrTiAl1Y compared to the parent alloy (see Table 2). In fact, NbMoCrTiAl1Y shows oxidation kinetics obeying to a quartic rate law (n = 4.5) in this stage indicating highly protective oxide scales, whereas NbMoCrTiAl0.5Y exhibits near-parabolic kinetics (n = 1.7). However, the stage II is slightly longer for the alloy with 0.5 at.% Y than that with 1 at.% Y. The stage III of all alloys is characterized by accelerated oxidation and oxidation rate exponents near or below 1. It should be pointed out that the time to breakaway oxidation, i.e. the transition from stage II to stage III oxidation, apparently decreases with increasing Y-content. Further, the oxidation kinetics of the Y-free alloy becomes only slightly faster in the III stage after approximately 8.5 h of oxidation, while the oxidation rates of the Y-containing alloys increase dramatically. Finally, the alloy with the highest Y content exhibits the highest mass gain and consequently the highest oxidation rate in the stage III, while the Y-free alloy possesses the lowest corresponding values.

In Fig. 4, the mass change curves of the cyclic oxidation of alloys NbMoCrTiAl and NbMoCrTiAl1Y at 1000°C as linear plots are displayed and the corresponding oxidation rates are listed in Table 2. The cycling oxidation experiments were stopped after 20 cycles, including 20 h in furnace in total and 5 h in the cooling zone. The Y-free alloy exhibits overall lower mass gain up to 10 cycles compared to the Y-added alloy. However, as marked by the arrows in Fig. 4, abrupt increase of mass change already after three cycles indicates a much earlier transition to stage III oxidation for the Y-free alloy. In contrast, the mass gain rate of the Y-added alloy continuously decreases up to 18 cycles of oxidation, indicating the formation of closed, protective oxide scales. As marked by the blue arrow in Fig. 4, the cyclic oxidation experiment was stopped right at the end of stage II oxidation for NbMoCrTiAl1Y. Comparing the oxidation kinetics of the isothermal and cyclic oxidation experiments (see Table 2), a short interval of parabolic oxidation can be observed for NbMoCrTiAl (n = 2.5) followed by a linear oxidation period with lower oxidation rates during cyclic oxidation compared to the isothermal conditions. Although the parabolic period during cyclic oxidation of NbMoCrTiAl is relatively short, the parabolic oxidation rate is lower compared to the Y-added alloy.

Table 2: Oxidation rate exponents (n) with regression coefficient (R^2) and n-dependent oxidation constants k_n, derived from a double-logarithmic plot using eq. (2). The subscripts l, p and q were used to define linear ($0.5 < n < 1.5$), parabolic ($1.5 < n < 2.5$)- and quartic ($3.5 < n < 4.5$) oxidation constant, respectively. Oxidation rates with corresponding rate exponents outside the definition range ($n < 0.5$) are designated with the subscript n.

alloy	stage	duration [h]	n	R^2	oxidation rate k_n
Isothermal Oxidation					
NbMoCrTiAl	II	1.7-8.5	1.5	0.98	$k_l = 1.2 \cdot 10^{-01}$ mg/cm^2·h
	III	8.5-48	0.8	0.99	$k_l = 3.5 \cdot 10^{-01}$ mg/cm^2·h
NbMoCrTiAl0.5Y	II	1.5-21	1.7	0.98	$k_p = 2.0 \cdot 10^{-01}$ mg^2/cm^4·h
	III	21-48	0.4	0.99	$k_n = 6.4 \cdot 10^{-02}$ mg^n/cm^{2n}·h
NbMoCrTiAl1Y	II	1.7-18	4.5	0.99	$k_q = 8.9 \cdot 10^{-01}$ mg^4/cm^8·h
	III	18-48	0.4	0.99	$k_n = 9.0 \cdot 10^{-02}$ mg^n/cm^{2n}·h
Cyclic Oxidation					
NbMoCrTiAl	II	1.4-3.2	2.5	0.97	$k_p = 2.3 \cdot 10^{-02}$ mg^2/cm^4·h
	III	3.2-25	0.8	0.98	$k_l = 1.3 \cdot 10^{-01}$ mg/cm^2·h
NbMoCrTiAl1Y	II	6.2-25	1.6	0.98	$k_p = 1.4 \cdot 10^{-01}$ mg^2/cm^4·h

Corrosion products

To identify the corrosion products of the oxidized samples, XRD measurements on NbMoCrTiAl, NbMoCrTiAl0.5Y (results are not shown here) and NbMoCrTiAl1Y after 10 min, 3 h and 24 h of exposure to air at 1000°C were conducted (see Fig. 5). After the shortest oxidation time, all alloys show the formation of mainly rutile-type oxides (ICSD Code 9161), only small Bragg peaks of Y_2O_3 (ICSD Code 23811) are visible in the diffraction pattern of NbMoCrTiAl1Y. Further oxides, namely Al_2O_3 (ICSD Code 88027) and Cr_2O_3 (ICSD Code 167268), which possibly form corundum solid solutions, were identified after 3 h of oxidation. For all alloys the formation of $CrNbO_4$ (ICSD Code 72275) and Nb_2O_5 (ICSD Codes 29, 17027) after 3 h and 24 h of oxidation can be confirmed. Interestingly, $YNbO_4$ (ICSD Code 239207) was additionally found after 3 h and 24 h of exposure in both Y-containing alloys. After 24 h of oxidation, the rutile-type oxides are the dominant oxides according to the XRD analysis.

The surface morphologies of the alloys NbMoCrTiAl and NbMoCrTiAl1Y after 6h of isothermal oxidation at 1000°C in air are shown in Figs. 6 (a) and 6 (b), respectively. EDX measurements (not shown here) reveal the formation of Ti-rich oxide on the surface. The oxides formed on top of the pegs further show high concentrations of Al and Y. The oxide scale formed on NbMoCrTiAl exhibits cracks suggestive of poor adherence, especially at the sample corners. The Y-containing alloy shows, on the contrary, a less defective scale with only few cracks. Further, hillocks are clearly visible (see Fig. 6 (b)) which result from the oxidation of the Al_2Y phase as revealed by means of cross-section micrographs and EDX-measurements (see for example Fig. 8 (c)).

Macroscopic and microscopic images of the surfaces after cyclic oxidation of the alloys NbMoCrTiAl and NbMoCrTiAl1Y are displayed in Fig. 6 (c) and 6 (d), respectively. The oxide scale of the Y-free alloys shows a severe tendency to spallation (see Fig. 6 (c)). By contrast, the oxide scale of the alloy NbMoCrTiAl1Y does not show any signs of cracks or spallation.

The oxidation behavior of the alloy NbMoCrTiAl at 1000°C in air has been investigated and can be found in [22, 25, 27]. In this study, only selected results are briefly presented. The BSE-image of NbMoCrTiAl after 10 min of exposure to air at 1000 °C shows an adherent multi-layered 2.3 µm thin oxide scale and an internal corrosion zone 4.4 µm in thickness (see supplementary materials Fig. S1). After 6 h of oxidation, oxide scales of various thicknesses (in average 41 µm) consisting of rutile-type oxides are formed beside to comparably thin regions of the scales (see Fig. 7 (a)). In Fig. 7 (b), the BSE cross-section image of relatively thin scales formed on the alloy NbMoCrTiAl after 24h oxidation at 1000 °C in air is displayed. In fact, the same corrosion products were identified compared to those formed after 6 h of oxidation, However, the amount of thick and porous regions is increased significantly. As marked in the images, the thick oxide scales are composed of rutile-type oxide rich in Ti, Nb, Cr and Al. The comparably thin oxide scales exhibit a multi-layer structure including an outer TiO_2 layer and an inner layer composed of Al_2O_3, Cr_2O_3, $CrNbO_4$ and Nb_2O_5 (see also [22, 25, 27]). Below the oxide scale, internal corrosion zone indicated by needle-shaped Al_2O_3 and spherical TiN particles was identified. Besides, minor amounts of other nitrides like Cr_2N were confirmed by XRD in our previous studies [22, 25].

The morphologies and the structures of the oxide scales formed on both Y-containing alloys are very similar. Therefore, results of the microstructural investigations of only the alloy NbMoCrTiAl1Y are shown here. Figure 8 (a) shows the BSE cross-section image of NbMoCrTiAl1Y after 10 min of exposure to air at 1000 °C. The results of the XRD- and EDX-analyses (see Fig. 5 and supplementary materials Fig. S2) reveal (similar to the Y-free alloy) the formation of an outer rutile-type TiO_2 oxide scale. Below, an Al_2O_3 scale was identified. At the metal/oxide interface, the formation of Nb and Ti-rich oxides with rutile-type structure and Nb_2O_5 was observed. After 6 h of exposure to air at 1000 °C, an oxide layer consisting of rutile-type $CrNbO_4$ and TiO_2 with embedded Al_2O_3 particles is clearly visible below the outer TiO_2 scale (see Fig. 8 (b) and supplementary materials Fig. S3). Interestingly, near the metal surface and close to $CrNbO_4$, Y-rich oxides were identified which, according to the results of the XRD measurements, were Y_2O_3 and $YNbO_4$. Obviously, the Al_2Y phase rapidly oxidizes to yttria and alumina forming pegs between metal and the oxide scale. With prolonged oxidation time, the oxide scales consisting of mainly rutile-type mixtures of Nb, Ti, Cr and Al oxides (see Fig. 8 (c), 8 (d) and supplementary material Fig. S4) become highly porous. According to the results of the EDX measurements, the Mo content in the oxide scale yields a negligibly low value. Apparently, Mo oxidizes to the volatile MoO_3 which was found as white needle-shaped particles in the reaction chamber after cooling. The internal corrosion zone consists, similar to the alloy NbMoCrTiAl, of needle-shaped Al_2O_3 and round-shaped TiN precipitates. Also, the internal corrosion along the Al_2Y phase boundaries is clearly visible and marked as “corrosion-path” in Fig. 8 (d).

BSE cross-section images of the alloys NbMoCrTiAl and NbMoCrTiAl1Y after the cyclic oxidation experiments (25h is the total test duration including 20h at 1000°C and 5h at RT) are displayed in Figs. 9 (a) and 9 (b), respectively. The oxide scale formed on NbMoCrTiAl is much thicker (~60 µm) and more porous than that formed on NbMoCrTiAl1Y (10-25 µm). According to the XRD and EDX investigations, the porous oxide layer on NbMoCrTiAl consists of Ti-, Nb-, Cr-, Al-rich rutile-type oxides (see supplementary materials Fig. S5). The oxide layer observed on the alloy NbMoCrTiAl1Y generally resembles in appearance the one formed during the short-time isothermal oxidation. At the metal/oxide interface, big pegs - oxidized regions of the former Al_2Y phase - are clearly seen. These pegs consist, according to the EDX-investigation, of Al and Y-rich oxides (see Fig. 9 (c)). It can be assumed that the pegs contribute to the good adherence of the oxide scale. At the interface metal/oxide, Cr-, Nb- and Ti-rich mixed oxide layer were detected in addition to the pegs (Fig. 9 (b)-(c)).

Discussion

The results presented above reveal that the addition of 0.5 at.% and 1 at.% Y to NbMoCrTiAl significantly alters the alloy microstructure. The solubility of Y in the bcc phase of pure Nb, Mo and Ta is known to be below 0.1 at.% even at temperatures of about 1000°C [28, 29]. Further, in the Al-Y system, Al_2Y possesses a very high thermodynamic stability and solidus temperature of 1500°C. It is therefore conclusive that precipitates of Al_2Y phase form even in the alloy with the lowest Y-concentration of 0.5 at.%.

The Y additions also significantly influence the oxidation behaviour of the studied alloys. Oxide scales formed on the Y-containing alloys are rather complex. In addition to TiO_2, Nb_2O_5, Al_2O_3, Cr_2O_3, MoO_3, $CrNbO_4$, which were found as corrosion products on the Y-free alloy, Y_2O_3 and $YNbO_4$ were identified on the Y-containing alloys. Y_2O_3 and $YNbO_4$ form according to equation (3) and (4), respectively. These oxides were found at the metal/oxide interface, while yttria was also observed as fine precipitates within the scale.

$$4Al_2Y + 9O_2 = 4\ Al_2O_3 + 2Y_2O_3 \qquad (3)$$

$$1/2\ Y_2O_3(s) + 1/2\ Nb_2O_5\ (s) = YNbO_4\ (s) \qquad (4)$$

The standard free energies of formation of the relevant oxides at 1000°C were calculated using the commercial software FactSage. The results are summarized in Table 3. Interestingly, Y_2O_3, Al_2O_3 and TiO_2 are by far the most stable oxides among the others. The rapid oxidation of Al_2Y according to equation (3) appears conclusive taking into account: (i) the high thermodynamic driving force for the formation of Y_2O_3 and Al_2O_3 and (ii) a high number of phase boundaries which offer fast diffusion paths.

Table 3: Standard free energy of formation of relevant oxides at 1000 °C

Oxide	**Cr_2O_3**	**Y_2O_3**	**TiO_2 (rutile)**	**Al_2O_3**	**MoO_3**	**Nb_2O_5**	**$YNbO_4$**	**$CrNbO_4$**
ΔG^0 [kJ/mol O_2]	-538	-1026	-713	-853	-293	-540	-783	-539

The standard free energy of formation of $YNbO_4$ was calculated considering equations (4) and (5) which were proposed in [30]. Apparently, the stability of $YNbO_4$ is substantially higher compared to that of Nb_2O_5 (see Table 3). Therefore, it is not surprising that $YNbO_4$ was found at the interface oxide/metal (see Fig.8 (b)). In our previous studies on NbMoCrTiAl [25], it was concluded that rapid growth of oxides scales is mainly attributed to the formation of Nb_2O_5 accompanied by high volume expansion and growth stresses [31–34]. It can be speculated that the formation of denser and slowly growing $YNbO_4$ instead of Nb_2O_5 has a positive effect on the oxidation of the Y-containing alloys as $YNbO_4$ increases the fracture toughness of the oxide scale. It was found that the ability to absorb cyclic stress, i.e. the damping capacity, of Nb_2O_5-type ceramics can be improved by sintering with Y_2O_3 forming a rutile-type oxide mixture of 95% $YNbO_4$ [30, 35].

$$\Delta G_{YNbO4} = 1/2\ (\Delta G_{Y2O3} + \Delta G_{Nb2O5}) \qquad (5)$$

As discussed in the previous section, the oxidation behaviour of the Y-free and Y-containing alloys during isothermal oxidation can be divided into three periods characterized by different oxidation kinetics. During transient oxidation, the mass gains of the Y-containing alloys are clearly higher compared to those of the Y-free alloy. Microscopic investigations (see supplementary materials Fig.

S8) reveal very fast oxidation of the Al_2Y phase forming stable oxides Al_2O_3 and Y_2O_3 (see Table 3) which clearly account for the higher values of the mass gain of the Y-containing alloys. With progressive oxidation time, i.e. in the stage II, a semi-continuous alumina layer probably effectively decreases the oxygen inward diffusion and reasons the lower oxidation kinetics observed in Y-containing alloys (see Figs. 3, 8 (b) and 9). A similar phenomenon was also found in other alloy systems. For example, Y promotes an accelerated formation of alumina on Ti48Al8Nb alloy [20, 21]. After prolonged oxidation, i.e. during stage III, the oxidation rates increase for all alloys, for Y-containing alloys, however, particularly dramatically. The Al_2Y phases at the metal/oxide interface seems to play a crucial role as its oxidation causes high local stresses in the vicinity of the Al_2Y phase provoking crack formation and, finally, massive oxygen ingress. Similar effects have been reported by Zhao et al. [20]. They investigated the microstructure and high temperature oxidation behaviour of Ti-45Al-8Nb alloy with various Y additions between 0.1 and 1 at.%. It was found that Y-concentrations above 0.1 at.% result in the precipitation of the Al_2Y phase along the grain boundaries. The high-temperature corrosion resistance of alloys was increased by Y concentrations between 0.2 and 0.3 at.%. Lower Y contents had virtually no effect, while Y contents above 0.3 at.% led to pronounced internal corrosion and provoked severe scale spallation.

Regarding the oxidation rate exponents of the alloys, a significant deviataion from the ideal linear or parabolic rate laws was observed. Linear oxidation refers to the formation of non-protective oxide scales which exhibit cracks or flaws. Therefore, the oxidation rate is limited primarily to the phase boundary reaction. Parabolic kinetics indicate that the oxidation process is governed by the diffusivity of ionic and electronic species through the oxide scale. In case of NbMoCrTiAl1Y for example a quartic oxidation rate exponent was measured during isothermal oxidation. Interestingly, quartic oxidation rates were observed during oxidation of various high-entropy alloys, such as TaMoCrTiAl ($n = 4.6$) [25], TaMoCrAl ($n = 4.4$) [25] and Cr-17.6Al-20.3Mo-15.2Nb-2.9Si-13.4Ta-5.4Ti ($n = 4.3$) [36]. As mentioned in the works of Lo et al. [36], these significant deviations from the ideal parabolic case might be attributed to the evaporation of gaseous specious such as MoO_3 [37] which was identified as white-yellowish precipitate in the furnace. Apparently, evaporation of MoO_3, even in low contents, affects the mass change recorded during oxidation experiments suggesting lower values of mass gain which, in turn, result in atypical oxidation rates such as quartic law observed in this work. Obviously, the determination of the correct oxidation rates of our RHEA that may potentially form MoO_3 needs additional thorough studies that will be performed in our future research. As a first approach, a method proposed by Azim et al. will be applied [38].

For the sake of comparison, the linear and parabolic oxidation rates of pure Ti, Nb as well as of an Al_2O_3- and a Cr_2O_3-forming Ni-based alloys are shown in Table 4. Obviously, the linear oxidation rates of Ti and Nb are significantly higher than those observed for NbMoCrTiAl with and without Y-additions (see Table 2). Possibly, the evaporation of MoO_3 reduces the linear oxidation rate of the high-entropy alloys while any evaporation effects can be excluded during oxidation of Ti or Nb at 1000 °C in air. The parabolic oxidations rates observed during oxidation of the Y-free and Y-added NbMoCrTiAl alloys are comparable to that of a Cr_2O_3-forming Ni-based alloy whereas the alumina forming alloy exhibits a significantly lower oxidation rate. In fact, this is not surprising as none of the alloys developed a fully-closed alumina scale during high-temperature oxidation although the alumina scales on the Y-added alloys appeared more distinctive in the cross-section micrographs (see for example Fig.9 (b)). Again, it should be pointed out that the comparison of oxidation rates of RHEA with those of Ni-based alloys should be considered critically because of the evaporation of MoO_3 that may occur during oxidation of RHEA.

Table 4: Data on oxidation kinetics of Ti, Nb and two Ni-based alloys IN718 (Cr_2O_3-former) and DD32 (Al_2O_3-former) at 1000 °C in air.

Substrate	k (mg^n/cm^{2n} h)	n	Reference
Ti (pure)	7.8	1.0	[39]
Nb (pure)	60.0	1.0	[40]
IN718 (Cr_2O_3-former)	$1.0 \cdot 10^{-01}$	2.0	[41]
DD32 (Al_2O_3-former)	$6.5 \cdot 10^{-05}$	2.0	[42]

During cyclic oxidation (within the I and II stages of the corresponding isothermal oxidation), adherent and protective oxide layers form on the alloy NbMoCrTiAl1Y, while the Y-free alloy exhibits loose, exfoliating and non-protective scales. The Al_2Y phase oxidizes quickly forming pegs (see Fig. 9(b)) which apparently increase the oxide scale adherence. This hypothesis can be support by experimental observation on Ti48Al8Nb-Y and Ti-Al-Y alloys where rapid oxidation of Al_2Y led to the formation of oxide pegs improving the scale adherence [18–21]. In Fig. 10, the stages I-III and their characteristic features occurring during isothermal oxidation of the Y-containing NbMoCrTiAl alloys are schematically summarized.

It can be concluded that Y generally has an ambivalent effect on the oxidation behaviour of the NbMoCrTiAl alloys. Initially, the fast oxidation of Al_2Y creates pegs between the oxide/metal interface enhancing the scale adherence. Further, the formation of $YNbO_4$ instead of the fast-growing Nb_2O_5 reduces oxidation rate and increases the scale cohesion. However, during the steady-state regime further oxidation of Al_2Y increases local growth stresses within the metal/oxide interface leading to crack formation and partial scale delamination. It can be assumed that a reduction of the Y concentration up to about 0.1 at.% to supress the formation of the Al_2Y in the alloy Nb-Mo-Cr-Ti-Al might improve its oxidation behaviour.

Conclusions

Based on results and discussion presented above, following conclusions can be drawn:

(i) The addition of Y leads to the formation of a highly stable Al_2Y phase but suppresses the formation of the intermetallic phase $Al(Mo,Nb)_3$ A15 in the equiatomic alloy NbMoCrTiAl.

(ii) The results of the isothermal oxidation reveal lower oxidation rates of the Y-containing alloys in the initial stage because of the formation of $YNbO_4$ within the multi-phase oxide layer instead of the quickly growing Nb_2O_5 that forms on the Y-free alloy.

(iii) During the steady-state oxidation, the severe oxidation of Al_2Y leads to crack formation and oxide failure.

(iv) The rapid oxidation of Al_2Y causes the formation of pegs at the metal/oxide interface accounting for the good scale adhesion during cyclic oxidation.

(v) To suppress the formation of Al_2Y in the equiatomic alloy NbMoCrTiAl, the concentration of Y should be reduced, presumably up to 0.1 at.%.

Acknowledgment

The financial support by the Deutsche Forschungsgemeinschaft (DFG), grant nos. GO 2283/2-1, GO 2283/4-1, HE 1872/31-1 and HE 1872/34-1 is gratefully acknowledged. Part of this work was performed at the Micro- and Nanoanalytics Facility (MNaF) of the University of Siegen.

References

1. Yeh J-W, Chen S-K, Lin S-J, et al. Nanostructured High-Entropy Alloys with Multiple Principal Elements: Novel Alloy Design Concepts and Outcomes. Adv. Eng. Mater. 2004;6:299–303.
2. Yeh JW, Chen YL, Lin SJ, Chen SK. High-Entropy Alloys – A New Era of Exploitation. MSF. 2007;560:1–9.
3. Senkov ON, Woodward C, Miracle DB. Microstructure and Properties of Aluminum-Containing Refractory High-Entropy Alloys. JOM. 2014;66:2030–2042.
4. Senkov ON, Senkova SV, Dimiduk DM, Woodward C, Miracle DB. Oxidation behavior of a refractory NbCrMo0.5Ta0.5TiZr alloy. J Mater Sci. 2012;47:6522–6534.
5. Senkov ON, Miracle DB, Chaput KJ, Couzinie J-P. Development and exploration of refractory high entropy alloys—A review. J. Mater. Res. 2018;33:3092–3128.
6. Senkov ON, Wilks GB, Miracle DB, Chuang CP, Liaw PK. Refractory high-entropy alloys. Intermetallics. 2010;18:1758–1765.
7. Senkov ON, Wilks GB, Scott JM, Miracle DB. Mechanical properties of Nb25Mo25Ta25W25 and V20Nb20Mo20Ta20W20 refractory high entropy alloys. Intermetallics. 2011;19:698–706.
8. Senkov O, Isheim D, Seidman D, Pilchak A. Development of a Refractory High Entropy Superalloy. Entropy. 2016;18:102.
9. Jensen JK, Welk BA, Williams REA, et al. Characterization of the microstructure of the compositionally complex alloy Al 1 Mo 0.5 Nb 1 Ta 0.5 Ti 1 Zr 1. Scripta Materialia. 2016;121:1–4.
10. Liu CM, Wang HM, Zhang SQ, Tang HB, Zhang AL. Microstructure and oxidation behavior of new refractory high entropy alloys. Journal of Alloys and Compounds. 2014;583:162–169.
11. Zheng J, Hou X, Wang X, Meng Y, Zheng X, Zheng L. Isothermal oxidation mechanism of a newly developed Nb–Ti–V–Cr–Al–W–Mo–Hf alloy at 800–1200 °C. International Journal of Refractory Metals and Hard Materials. 2016;54:322–329.
12. Young DJ. High Temperature Oxidation and Corrosion of Metals. Burlington: Elsevier; 2008.
13. Kofstad P. High temperature corrosion. London: Elsevier Applied Science; 1988.
14. Bürgel R, Jürgen Maier H, Niendorf T. Handbuch Hochtemperatur- Werkstofftechnik. Wiesbaden: Vieweg+Teubner; 2011.
15. Whittle DP, Stringer J. Improvements in High Temperature Oxidation Resistance by Additions of Reactive Elements or Oxide Dispersions. Philosophical Transactions of the Royal Society of London. Series A, Mathematical and Physical Sciences. 1980;295:309–329.

16. Hou PY. The Reactive Element Effect – Past, Present and Future. MSF. 2011;696:39–44.

17. Naumenko D, Pint BA, Quadakkers WJ. Current Thoughts on Reactive Element Effects in Alumina-Forming Systems: In Memory of John Stringer. Oxid Met. 2016;86:1–43.

18. Wu Y, Hagihara K, Umakoshi Y. Influence of Y-addition on the oxidation behavior of Al-rich γ-TiAl alloys. Intermetallics. 2004;12:519–532.

19. Gong X, Chen RR, Fang HZ, et al. Synergistic effect of B and Y on the isothermal oxidation behavior of TiAl-Nb-Cr-V alloy. Corrosion Science. 2018;131:376–385.

20. Zhao LL, Li GY, Zhang LQ, et al. Influence of Y addition on the long time oxidation behaviors of high Nb containing TiAl alloys at 900 °C. Intermetallics. 2010;18:1586–1596.

21. Xiang LL, Zhao LL, Wang YL, Zhang LQ, Lin JP. Synergistic effect of Y and Nb on the high temperature oxidation resistance of high Nb containing TiAl alloys. Intermetallics. 2012;27:6–13.

22. Gorr B, Mueller F, Christ H-J, et al. High temperature oxidation behavior of an equimolar refractory metal-based alloy 20Nb 20Mo 20Cr 20Ti 20Al with and without Si addition. Journal of Alloys and Compounds. 2016;688:468–477.

23. Chen H, Kauffmann A, Gorr B, et al. Microstructure and mechanical properties at elevated temperatures of a new Al-containing refractory high-entropy alloy Nb-Mo-Cr-Ti-Al. Journal of Alloys and Compounds. 2016;661:206–215.

24. Chen H, Kauffmann A, Seils S, et al. Crystallographic ordering in a series of Al-containing refractory high entropy alloys Ta–Nb–Mo–Cr–Ti–Al. Acta Materialia. 2019;176:123–133.

25. Müller F, Gorr B, Christ H-J, et al. On the oxidation mechanism of refractory high entropy alloys. Corrosion Science. 2019;108161.

26. Gorr B, Mueller F, Christ H-J, et al. Development of Oxidation Resistant Refractory High Entropy Alloys for High Temperature Applications: Recent Results and Development Strategy. In: & Materials Society TM, ed. TMS 2018 147th Annual Meeting & Exhibition Supplemental Proceedings. Cham: Springer International Publishing; 2018:647–659.

27. Gorr B, Müller F, Azim M, et al. High-Temperature Oxidation Behavior of Refractory High-Entropy Alloys: Effect of Alloy Composition. Oxid Met. 2017;88:339–349.

28. Lundin CE, Klodt DT. Alloy Systems of Group VA Metals With Yttrium. Journal of the Institute of Metals. 1962;90:341–347.

29. English JJ, Defense Metals Information Center. Binary and ternary phase diagrams of columbium, molybdenum, tantalum, and tungsten. Columbus, Ohio: Defense Metals Information Center, Battelle Memorial Institute; 1961.

30. Nishiyama K, Abe T, Sakaguchi T, Momozawa N. Damping properties of YNbO4–Nb2O5–Y2O3 ceramics. Journal of Alloys and Compounds. 2003;355:103–107.

31. Thomas KS, Varma SK. Oxidation response of three Nb–Cr–Mo–Si–B alloys in air. Corrosion Science. 2015;99:145–153.

32. Varma SK, Parga C, Amato K, Hernandez J. Microstructures and high temperature oxidation resistance of alloys from Nb–Cr–Si system. J Mater Sci. 2010;45:3931–3937.

33. Ercit TS. Refinement of the structure of ?-Nb2O5 and its relationship to the rutile and thoreaulite structures. Mineralogy and Petrology. 1991;43:217–223.

34. Arbuzov MP, Chupria VG. The oxidation of niobium and the structure of niobium oxides. Sov. Phys. J. 1965;8:87–89.

35. Cabral RF, Prado da Silva MH, Campos JB de, Lima ES. Study of the Sintering of Mixtures Al_2O_3-Nb_2O_5 and Y_2O_3-Nb_2O_5. MSF. 2012;727-728:799–803.

36. Lo K-C, Murakami H, Yeh J-W, Yeh A-C. Oxidation behaviour of a novel refractory high entropy alloy at elevated temperatures. Intermetallics. 2020;119:106711.

37. Gulbransen EA, Andrew KF, Brassart FA. Oxidation of Molybdenum 550° to 1700°C. J. Electrochem. Soc. 1963;110:952.

38. Azim MA, Gorr B, Christ H-J, Heilmaier M, Koch U, Engelhard M. Characterization of Oxidation Kinetics of Mo–Si–B-Based Materials. Oxid Met. 2017;87:89–108.

39. Kofstad P, Anderson PB, Krudtaa OJ. Oxidation of titanium in the temperature range 800–1200°C. Journal of the Less Common Metals. 1961;3:89–97.

40. Kofstad P, Kjollesdal H. Oxidation of niobium (columbium) in the temperature range 500 to 1200°C. Transaction Metallurgical Soc. AIME. 1961;221:285.

41. Greene GA, Finfrock CC. Oxidation of Inconel 718 in Air at High Temperatures. Oxid Met. 2001;55:505–521.

42. Liu CT, Ma J, Sun XF. Oxidation behavior of a single-crystal Ni-base superalloy between 900 and 1000°C in air. Journal of Alloys and Compounds. 2010;491:522–526.

Figures

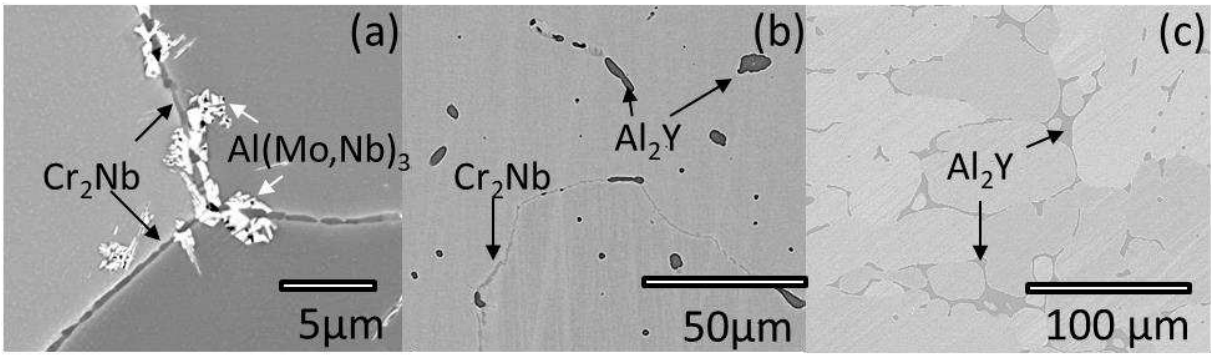

Fig.1: SEM images (BSE contrast) of (a) NbMoCrTiAl, (b) NbMoCrTiAl0.5Y, and (c) NbMoCrTiAl1Y.

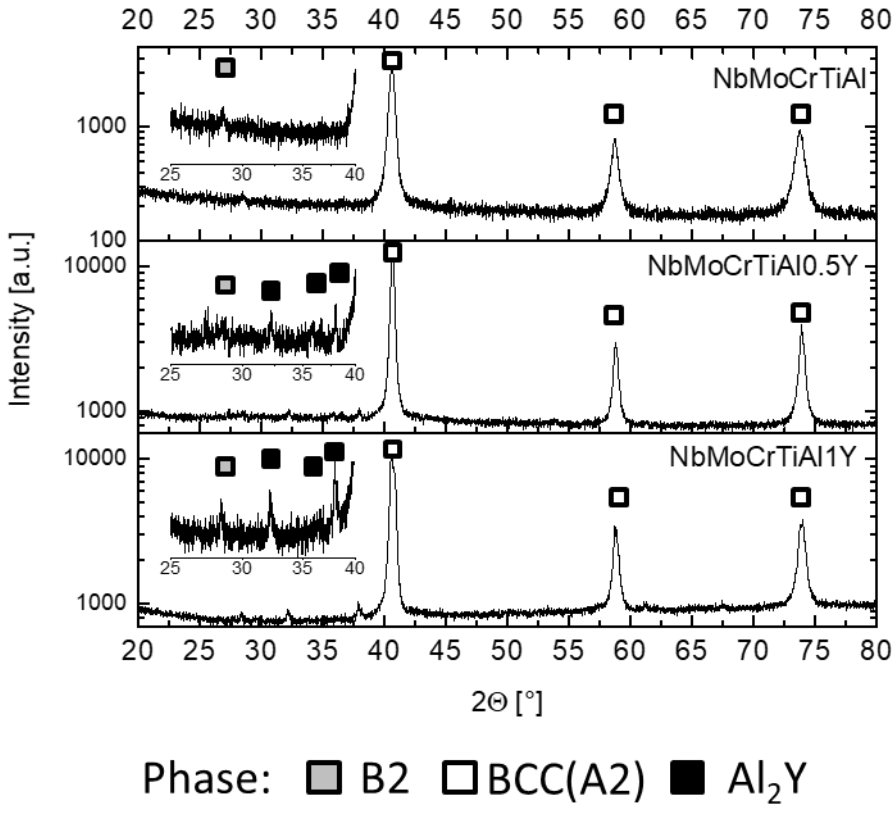

Fig.2: Powder XRD patterns of NbMoCrTiAl, NbMoCrTiAl0.5Y, and NbMoCrTiAl1Y.

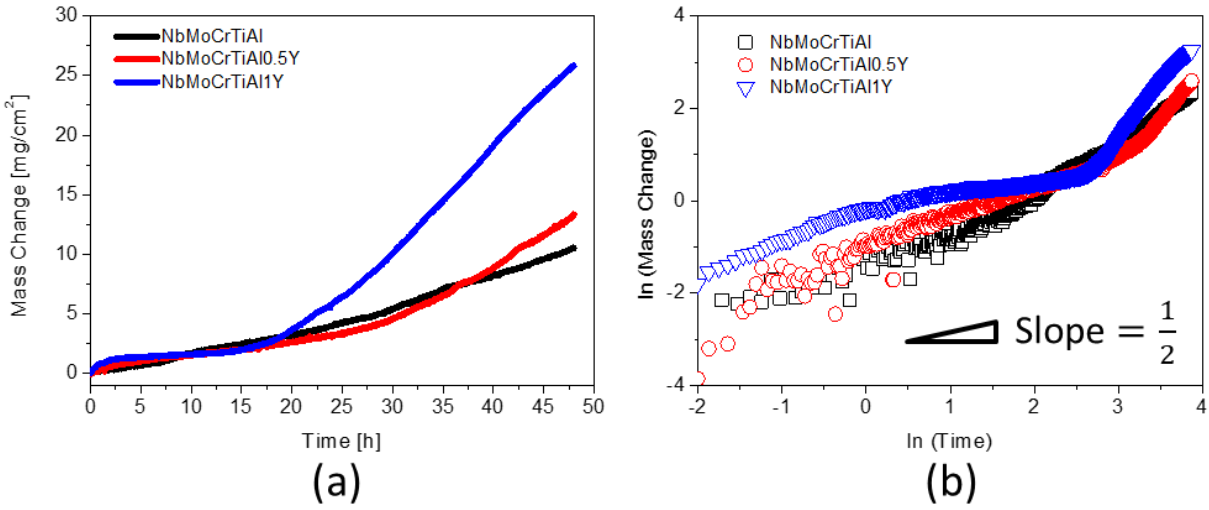

Fig. 3: Oxidation kinetics of NbMoCrTiAl, NbMoCrTiAl0.5Y and NbMoCrTiAl1Y during isothermal exposure to air at 1000°C; (a) mass change curves and (b) double-logarithmic plots of mass change against time.

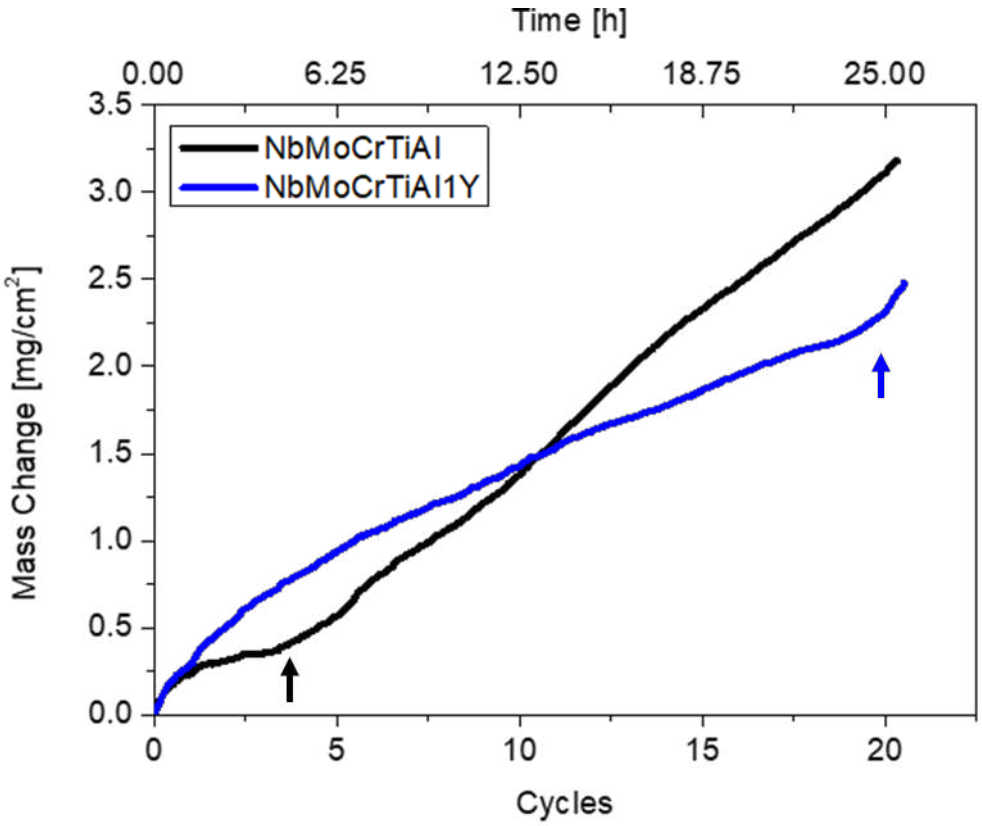

Fig. 4: Linear Mass change curves against time for NbMoCrTiAl and NbMoCrTiAl1Y during cyclic oxidation at 1000°C in air. The arrows mark the onset of stage III oxidation, i.e. transition to linear oxidation kinetics, for the corresponding alloys.

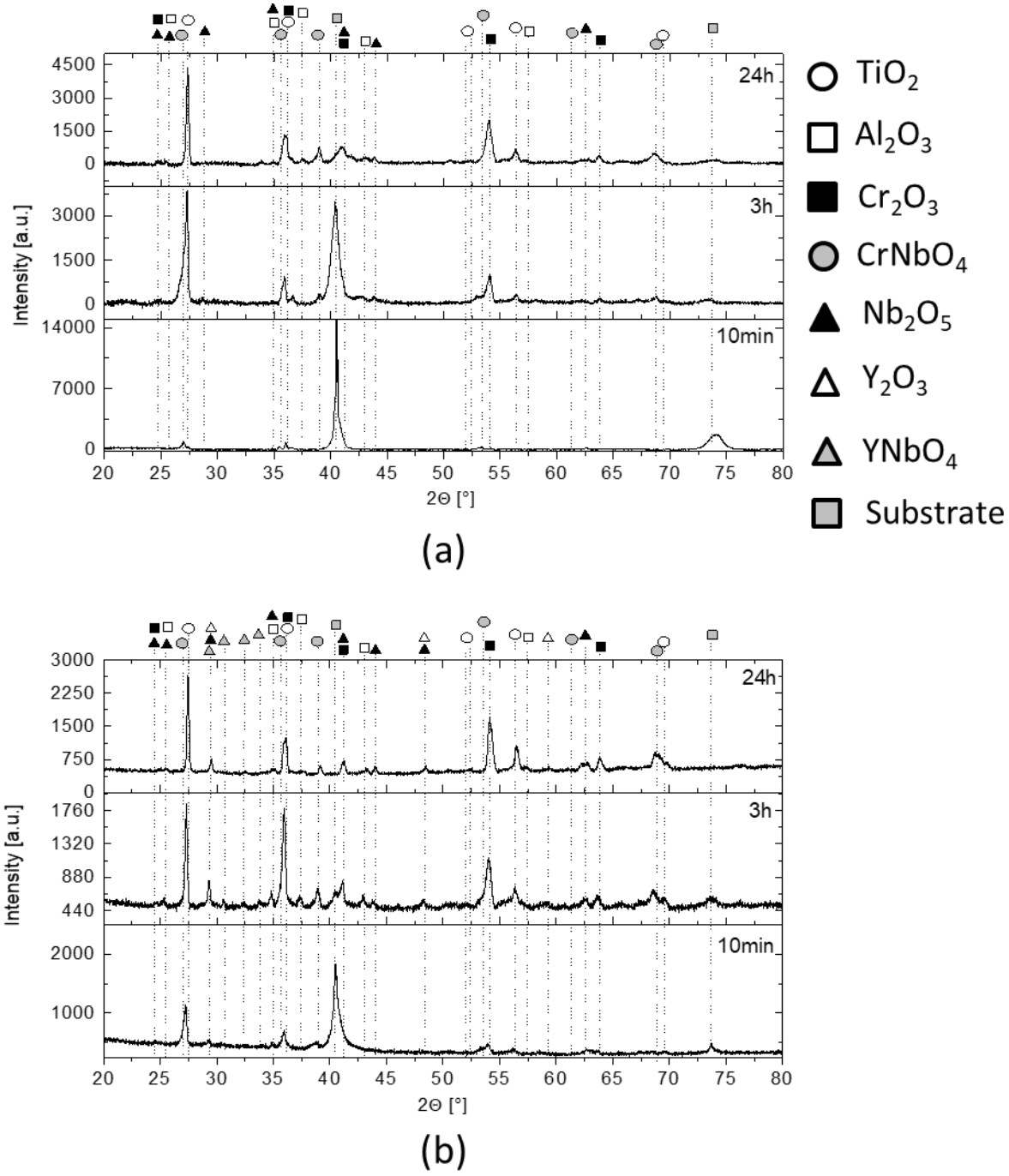

Fig.5 Results of the XRD analysis after 10min, 3h and 24h of exposure to air at 1000°C; (a) NbMoCrTiAl and (b) NbMoCrTiAl1Y.

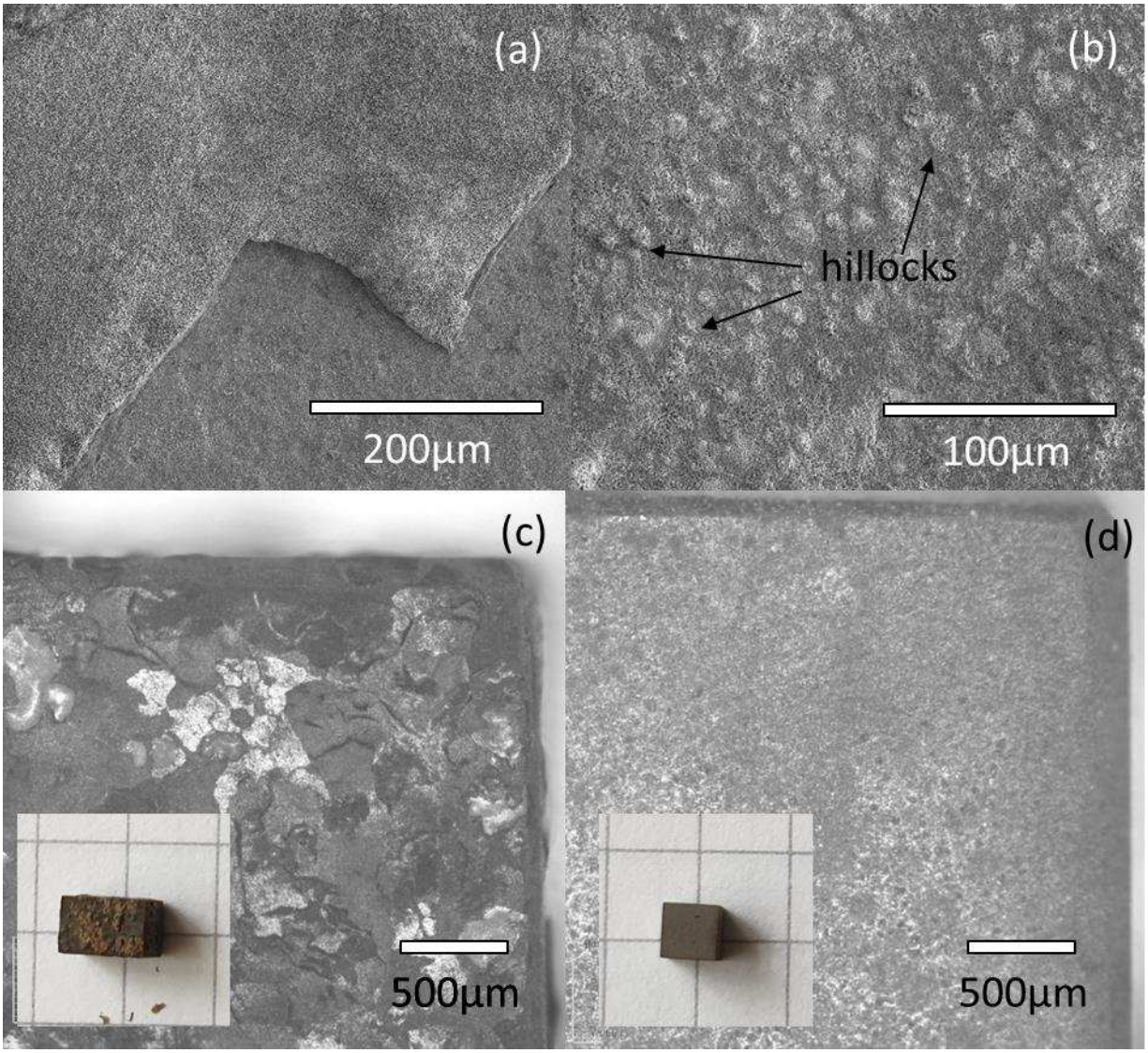

Fig. 6: Surface morphologies of NbMoCrTiAl and NbMoCrTiAl1Y (a), (b) after 6h of isothermal oxidation at 1000°C in air as well as (c), (d) after the cyclic oxidation experiments.

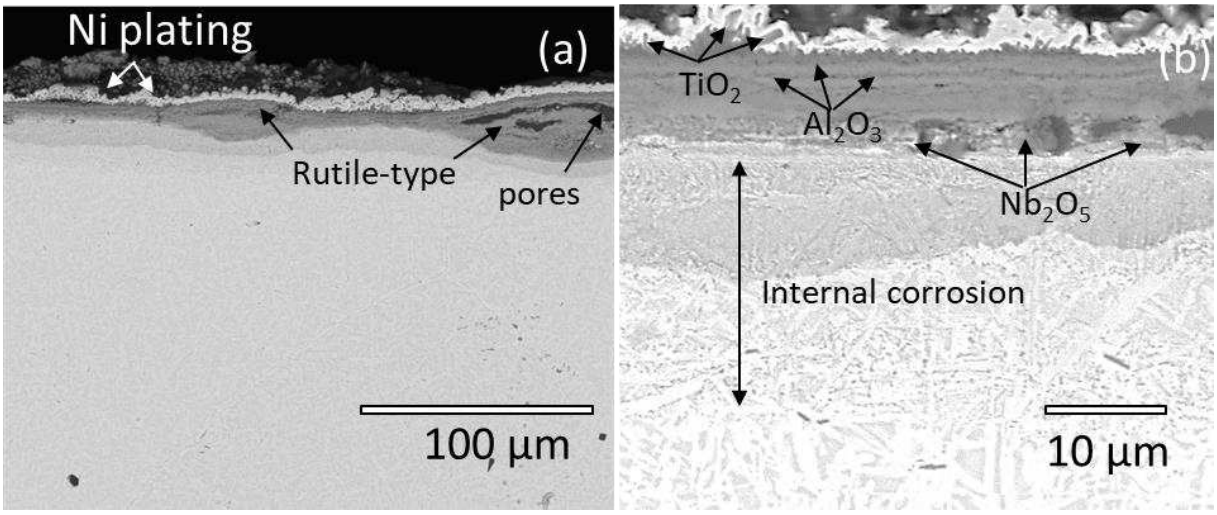

Fig. 7: Oxide scales formed on the alloy NbMoCrTiAl after oxidation at 1000°C; (a) BSE image after 6h of oxidation showing areas with thick and thin oxide scales and (b) high magnification image of a thin oxide scale formed after 24h of oxidation.

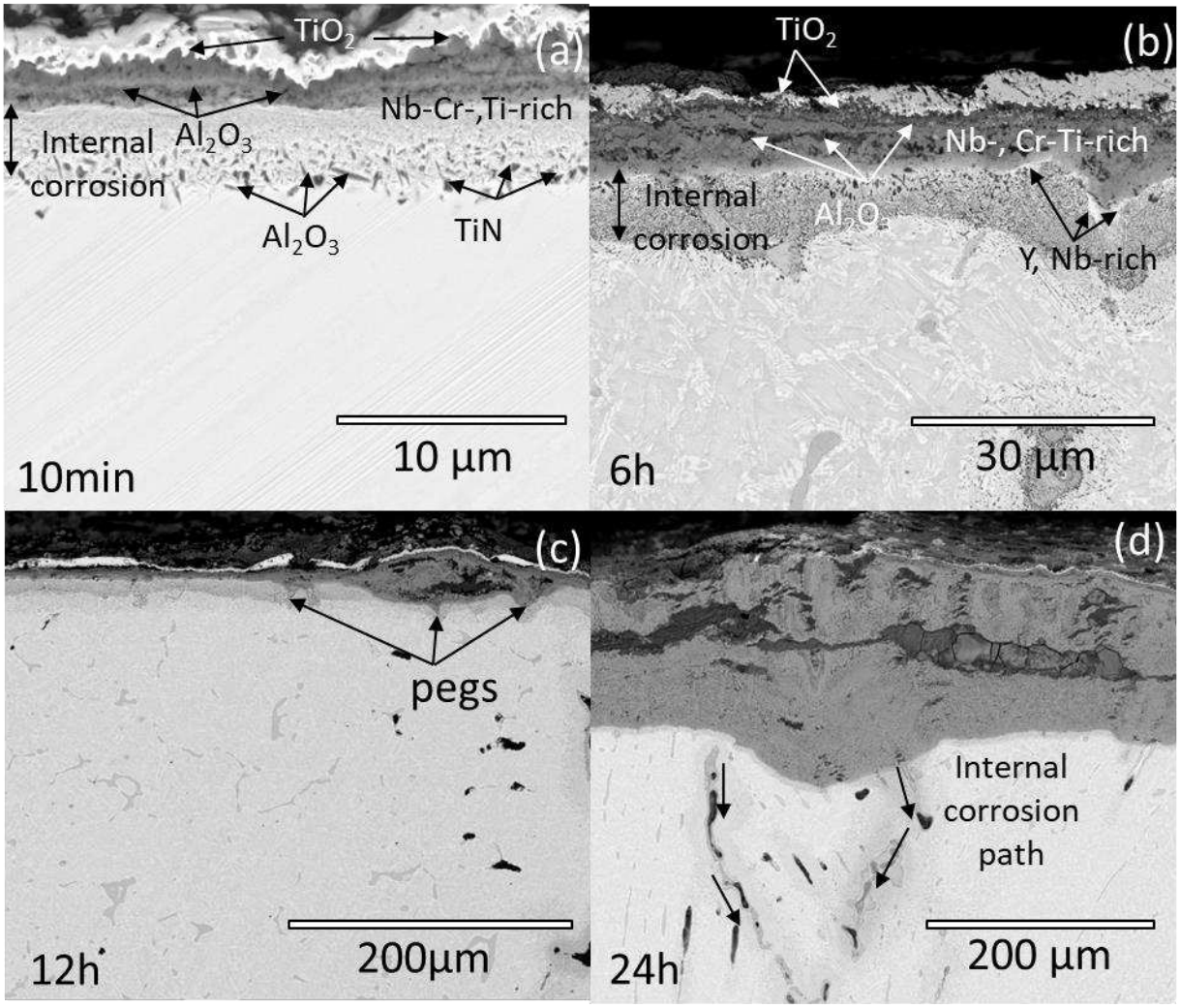

Fig 8: BSE cross-section image of NbMoCrTiAl1Y after isothermal oxidation (a) for 10min, (b) 6h, (c) 12h and (d) 24h at 1000°C in air.

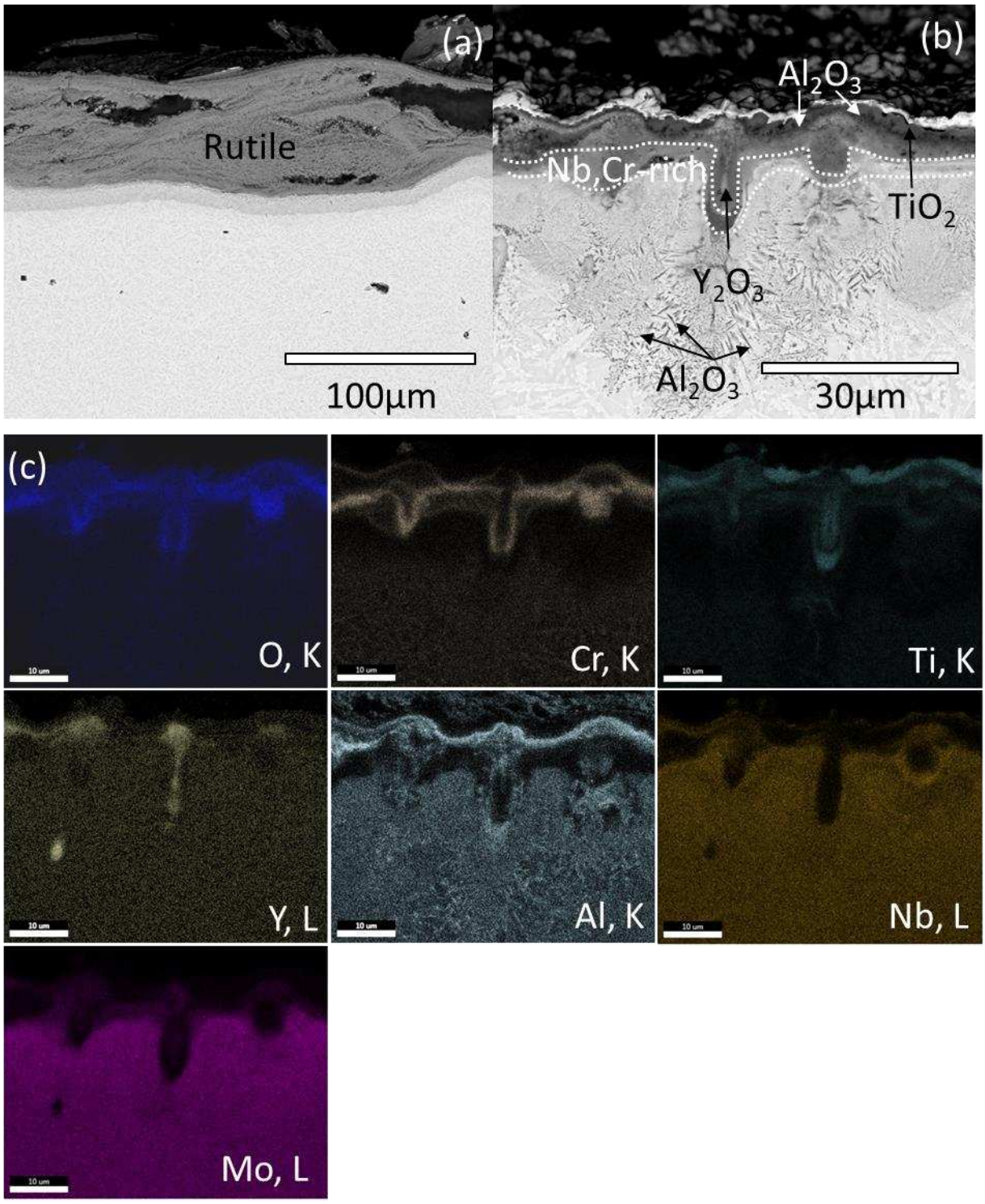

Fig. 9: Oxide scale formed after 24h of cyclic oxidation; (a) BSE cross-section of NbMoCrTiAl, (b) BSE cross-section of NbMoCrTiAl1Y and (c) corresponding EDX mapping of (b).

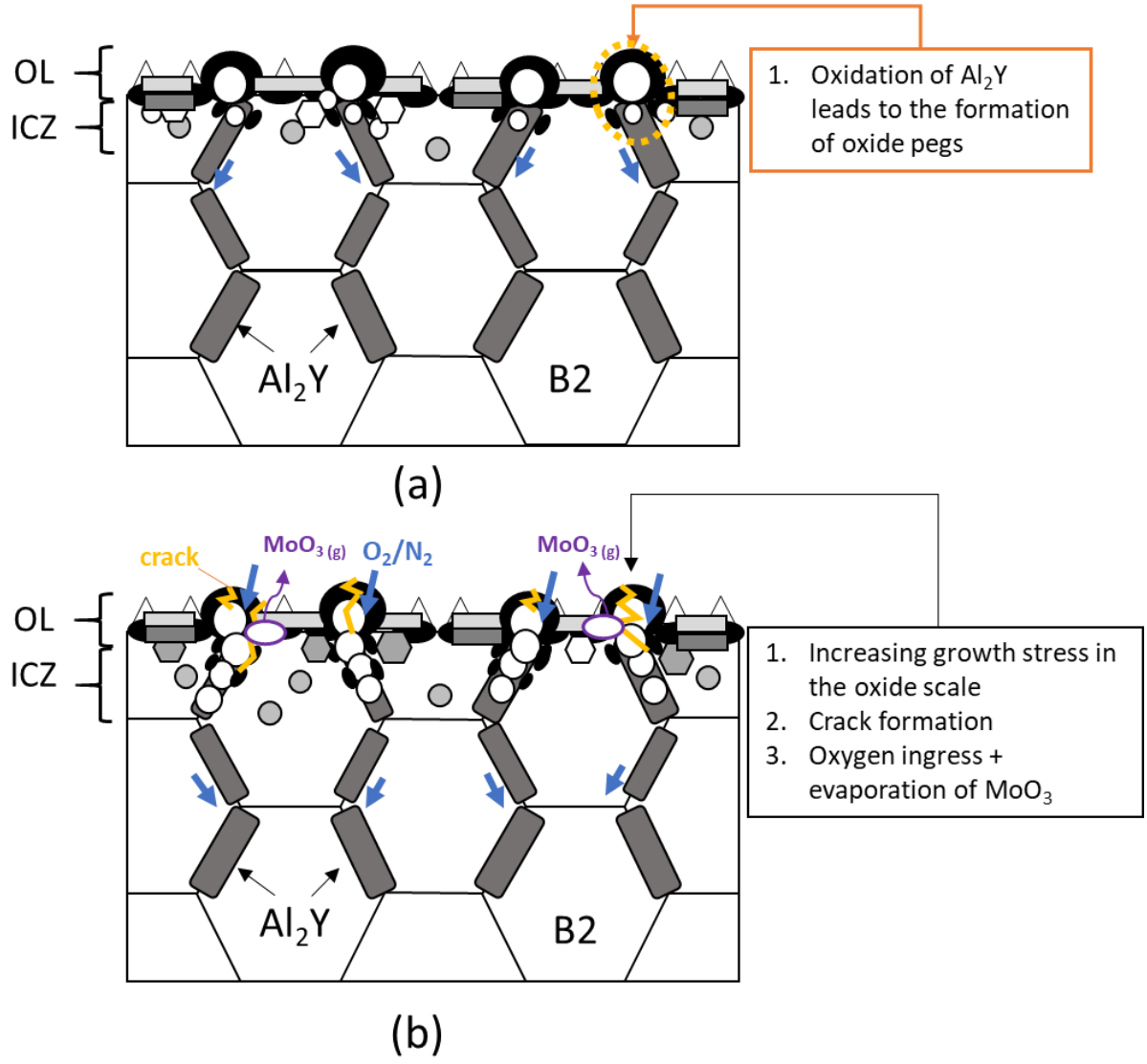

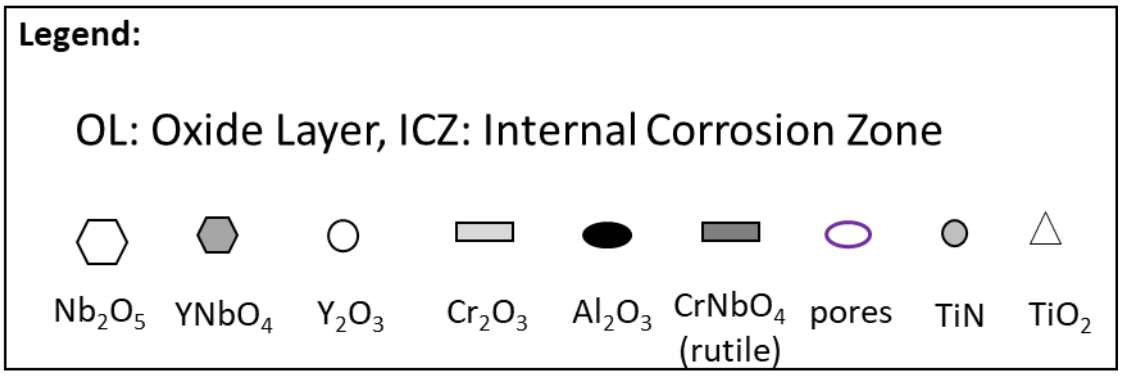

Fig. 10 Oxidation behavior of Y-containing NbMoCrTiAl alloys during oxidation at 1000°C. (a) Stage I + II: Formation of a protective multi-phase oxide layer and pegs, (b) Stage III: Oxidation along the Al_2Y phase provokes crack formation and failure of the protective oxide layer.